DOI: http://dx.doi.org/10.12989/was.2010.13.2.169
Wind and Structures, Vol. 13, No. 2 (2010) 169-189

Special Issue paper on Windborne Debris

CFD modelling of free-flight and auto-rotation of plate type debris

B. Kakimpa[1]*, D.M. Hargreaves[1], J.S. Owen[1], P. Martinez-Vazquez[2], C.J. Baker[2], M. Sterling[2] and A.D. Quinn[2]

[1]*Department of Civil Engineering, The University of Nottingham, University Park, Nottingham, NG7 2RD, UK*
[2]*School of Civil Engineering, The University of Birmingham, Edgbaston, Birmingham, B15 2TT, UK*

(Received September 18, 2009, Accepted January 2, 2010)

Abstract. This paper describes the use of coupled Computational Fluid Dynamics (CFD) and Rigid Body Dynamics (RBD) in modelling the aerodynamic behaviour of wind-borne plate type objects. Unsteady 2D and 3D Reynolds Averaged Navier-Stokes (RANS) CFD models are used to simulate the unsteady and non-uniform flow field surrounding static, forced rotating, auto-rotating and free-flying plates. The auto-rotation phenomenon itself is strongly influenced by vortex shedding, and the realisable k-epsilon turbulence modelling approach is used, with a second order implicit time advancement scheme and equal or higher order advection schemes for the flow variables. Sequentially coupling the CFD code with a RBD solver allows a more detailed modelling of the Fluid-Structure Interaction (FSI) behaviour of the plate and how this influences plate motion. The results are compared against wind tunnel experiments on auto-rotating plates and an existing 3D analytical model.

Keywords: CFD; autorotation; windborne debris; fluid-structure interaction.

1. Introduction

Wind borne debris is one of the major causes of building envelope failure during severe storms (Minor 1994). The determination of debris flight trajectories and impact kinetic energy are critical to debris risk management strategies. A number of analytical models describing the two- and three-dimensional trajectories of plates have been presented by Tachikawa (1983), Holmes (2004), Baker (2007), Richards, *et al.* (2008) and Martinez-Vazquez, *et al.* (2009a). These analytical models are based on the principles of linear and angular momentum conservation and rely on experimentally obtained static plate force coefficients to describe the aerodynamic characteristics of the plate. The FSI effects due to plate auto-rotation are described using Magnus force coefficients.

However, these analytical models are currently limited by not fully accounting for the effects on plate motion of intermittent flow separation and re-attachment and the unsteady turbulent flow phenomena that develop around the plate, such as vortex shedding. Also, the Magnus force

* Corresponding Author, E-mail: evxbk1@nottingham.ac.uk

assumption does not fully account for the non-linear FSI influencing plate motion. While the Magnus effect allows for estimation of the auto-rotational lift resulting from plate rotational, this is not the only FSI in question as the plate can undergo complex interactions with its own wake that affect force coefficients and rotational speed.

Fully coupled Computational Fluid Dynamics (CFD) and Rigid Body Dynamics (RBD) codes have been demonstrated to be useful tools for the study of rigid body dynamics problems involving detailed FSI. These include problems such as the shedding of foam debris from Space Shuttle Launch Vehicles during ascent (Murman, *et al.* 2005) and the dynamics of cylindrical mines dropping through the ocean (Mann, *et al.* 2007). Coupled CFD-RBD simulations have also been applied to efficiently generate force coefficients for use in the three-dimensional (3D) aerodynamic characterisation of rigid projectiles, and the simulation of their motion (Costello, *et al.* 2007). These studies have however focused on streamlined bodies flying at super-sonic speeds and at high altitudes, or dropping through water. Comparatively, plate free-flight and auto-rotation consists of non-streamlined objects flying at lower altitudes with sub-sonic speeds and exhibiting streamlined, transition, as well as bluff body flow. Therefore, although some insights might be obtained from these studies, their findings are not fully applicable to the study of plate type wind-borne debris. The ability of CFD-RBD simulations to contribute to the study of plate free-flight and auto-rotation is however adequately demonstrated. The advantages offered by these CFD-RBD models such as the rapid and relatively lower cost characterisation of different debris shapes and the investigation of a wide range of flow conditions and debris types are beneficial to the study of wind-borne debris flight. CFD-RBD simulations unlike the analytical model allow for the detailed study of the entire debris environment, while accounting for unsteady and turbulent flow effects and allowing a more detailed modelling of debris behaviour by capturing the FSI.

Previous studies on the CFD-RBD simulation of plate type wind-borne debris flight have focused on 2D CFD simulations and are summarised in Kakimpa, *et al.* (2009), with comparisons against existing analytical models of debris flight in Martinez-Vazquez, *et al.* (2009a). The findings of these studies highlight some of the limitations of 2D CFD-RBD simulations such as the over-prediction of drag and lift resulting from the suppression of 3D break-up of the flow in 2D CFD models, and the restriction of the plate from lateral displacements and rotations. There are also inaccuracies arising from the application of RANS turbulence models to bluff body flow when the plate is at high angles of attack. It is therefore necessary to extend the existing CFD-RBD work to allow for full 3D simulations of plate type debris.

This paper presents a full 3D CFD-RBD approach to debris flight modelling, using the ANSYS FLUENT (Fluent Inc. 2006) commercial CFD code, sequentially coupled with a full six degree of freedom RBD solver. Section 2 describes the CFD model used for these simulations, presenting descriptions of the domain and the various numerical and solution schemes used. Section 3 then presents the RBD model and discusses the CFD-RBD coupling framework used for this study. Section 4 discusses the results of fixed static plate CFD simulations performed to assess the performance of the CFD model and their comparison with experimental data.

During plate type debris flight however, the plates experience significant translations and rotations. This is accompanied by cycles of flow separation, reattachment and vortex shedding in its environment which in turn affects the instantaneous aerodynamic forces driving the plate's motion. This complex FSI is influenced by, among other factors, the plate rotational speed and has an impact on the debris flight behaviour. The model is applied to modelling these FSI effects in section

5 which presents the results of a set of simulations involving plate forced rotation at fixed rotational speeds. These were performed to assess the effects of increased rotational speed on plate force coefficients.

In reality however, plate rotation does not occur at a fixed speed but would undergo angular acceleration and deceleration during auto-rotation. Auto-rotation is defined as the continuous rotation, without external power of a body exposed to an air stream (Skews 1990; Smith 1971). This auto-rotation would also be three dimensional in nature and would not occur about only one single fixed axis as modelled in some previous experiments (Skews 1990; Smith 1971), but about all three orthogonal axes. Section 6 presents 3D CFD-RBD simulations of plate auto-rotation about only one horizontal axis through its centre. In order to assess the performance of the CFD-RBD model in simulating the plate's FSI behaviour, the results in section 6 are compared with measurements of an auto-rotating plate in the wind tunnel. Section 7 then presents demonstrative CFD-RBD simulations of full plate free-flight with combined translation and full three-dimensional auto-rotation. Finally conclusions and future work are presented in section 8.

2. CFD model description

The proprietary CFD code, ANSYS FLUENT (Fluent Inc. 2006) was used to solve the unsteady incompressible Navier-Stokes equations in order to simulate the flow field in the plate's environment. These equations are based on the principles of continuity (mass conservation) and momentum conservation. For the modelling of turbulent flows, where the flow variables such as pressure and velocity are characterised by temporal fluctuations, Reynolds decomposition is used to represent the instantaneous pressure and velocity signals. The instantaneous fluctuating signal for, say velocity (u_i), is decomposed into a time-averaged component (U_i), and a fluctuating component (u_i') as shown in Eq. (1):

$$u_i = U_i + u_i' \tag{1}$$

By ensemble averaging of the 3D Navier-Stokes equations with Reynolds decomposition applied to the flow variables, the 3D Reynolds-Averaged Navier-Stokes (RANS) equations (Eqs. (2) and (3) are obtained. Eq. (2) is the continuity equation, while Eq. (3) is the momentum conservation equation.

$$\frac{\partial U_i}{\partial x_i} = 0 \tag{2}$$

$$\rho\frac{\partial U_i}{\partial t} + \rho U_j\frac{\partial U_i}{\partial x_j} = -\frac{\partial P}{\partial x_i} + \frac{\partial}{\partial x_j}\left[\mu\left(\frac{\partial U_i}{\partial x_j} + \frac{\partial U_j}{\partial x_i}\right) - \overline{\rho u_j' u_i'}\right] \tag{3}$$

where U_i is the instantaneous time averaged velocity in the x_i direction, u_i' is the instantaneous fluctuating component of velocity in the x_i direction, P is the time averaged static pressure, μ is the fluid dynamic viscosity, ρ is the fluid density, and $-\overline{\rho u_j' u_i'}$ is the Reynolds stresses tensor denoted by τ_{ij}. This Reynolds stress tensor introduces six additional unknown terms (since $\tau_{ij} = \tau_{ji}$) into the RANS equations. The Boussinesq approximation is used to relate these Reynolds stresses to the mean rates of deformation according to Eq. (4):

$$-\overline{\rho u_j' u_i'} = \mu_t\left(\frac{\partial U_i}{\partial x_j} + \frac{\partial U_j}{\partial x_i}\right) - \frac{2}{3}k\delta_{ij} \tag{4}$$

where μ_t is the turbulent (or eddy) viscosity, k is the turbulent kinetic energy, and δ_{ij} is the Kroeneker delta function. A turbulence model is then used to solve for the eddy viscosity and turbulent kinetic energy in order to solve for the Reynolds stresses. A number of turbulence models exist and the choice of appropriate turbulence model is largely problem specific.

In the case of plate type debris flight, the auto-rotation phenomenon involved has been found to be strongly influenced by vortex shedding from the retreating faces of the plate (Lugt 1983) and the lift hysteresis resulting from unsteady aerodynamic effects (Smith 1971; Richards, *et al.* 2008). The flow around the plate also involves rotating flows and intermittent flow separation and reattachment. Detailed CFD studies were therefore carried out from a number of 2-equation eddy viscosity models and Reynolds Stress Transport Models (RSM) models in order to select a turbulence model that allows sufficiently accurate simulation of vortex shedding and intermittent flow separation and reattachment, while remaining computationally efficient. Table 1 shows the results of some of these studies from 2D CFD simulations on static plates. The results show that in terms of the steady state average drag predictions on a thin flat plate held normal to the flow, the Re-Normalisation Group k-ε (RNG k-ε), Realisable k-ε (R k-ε) and RSM turbulence models gave a similar degree of accuracy when compared against experimental data from ESDU (1970).

Ultimately, the realisable k-ε turbulence modelling approach by Shih, *et al.* (1995) was preferred due to the fact that it enforces mathematical constraints that ensure the turbulence is realisable, and hence possesses the minimal requirement to prevent a turbulence model from producing non-physical predictions. An enhanced wall function was applied for the near wall turbulence modelling (Fluent Inc. 2006).

In the realisable k-ε turbulence model, a mathematically derived equation for the transport of turbulent kinetic energy, k, (Eq. (5)) is solved together with an empirically derived equation for the dissipation rate, ε, (Eq. (6)).

$$\rho\frac{\partial k}{\partial t} + \rho U_j\frac{\partial k}{\partial x_j} = \frac{\partial}{\partial x_j}\left[\left(\mu + \frac{\mu_t}{\sigma_k}\right)\frac{\partial k}{\partial x_j}\right] + \mu_t S^2 - \rho\varepsilon \tag{5}$$

$$\rho\frac{\partial \varepsilon}{\partial t} + \rho U_j\frac{\partial \varepsilon}{\partial x_j} = \frac{\partial}{\partial x_j}\left[\left(\mu + \frac{\mu_t}{\sigma_k}\right)\frac{\partial \varepsilon}{\partial x_j}\right] + C_1\rho S\varepsilon - \rho C_2\frac{\varepsilon^2}{k + \sqrt{\nu\varepsilon}} \tag{6}$$

where S is the modulus of the mean rate of strain tensor and ν is the kinematic viscosity. For the

Table 1 Steady State CFD simulations for a thin flat plate normal to a flow of Re = 5.4×10^4

Turbulence model	Wall function	y^+_{avg}	$(C_d)_{avg}$	$(C_d)_{rms}$	$((C_d)_{CFD} - (C_d)_{expt})/(C_d)_{expt}$
S k-ε	Standard	3.949	2.240	3.50E-02	14.859%
S k-ε	Enhanced	3.774	2.243	3.54E-02	15.041%
RNG k-ε	Enhanced	3.781	2.011	3.50E-02	3.118%
R k-ε	Enhanced	3.644	2.042	1.05E-02	4.719%
RSM	Enhanced	3.610	1.890	3.18E-02	-3.094%

realizable k-ε model, C_1 is defined in Eq. (7):

$$C_1 = \max\left[0.43, \frac{\eta}{\eta + 5}\right] \tag{7}$$

where $\eta = Sk/\varepsilon$. The model constants; C_2, σ_k and σ_ε have been determined experimentally as 1.9, 1.0 and 1.2 respectively.

With values of k and ε obtained from solving Eqs. (5) and (6), the eddy viscosity is then computed as shown in Eq. (8):

$$\mu_t = \rho C_\mu \frac{k^2}{\varepsilon} \tag{8}$$

where in the realisable k-ε model, C_μ is not a constant but is computed from the mean strain and rate of rotation (Shih, *et al.* 1995).

The RANS and turbulence equations were solved using a Finite Volume algorithm with second order implicit time advancement and second order pressure and advection schemes. SIMPLE and PISO algorithms were used for pressure-velocity coupling.

Table 2 shows results from some of the studies performed on static 2D flat plates to assess the performance of various pressure, advection and P-V coupling schemes. The 1st order upwind scheme gave the most accurate drag predictions but did not adequately capture the associated flow mechanisms; the vortex shedding and its associated body force fluctuations were considerably dampened compared with the other models. Therefore in order to more adequately model the flow, a number of higher order advection scheme were assessed with a coupled flow solver used. These higher order advection scheme schemes included: 2nd order upwind, QUICK and 3rd order MUSCL schemes. The 3rd order MUSCL scheme performed marginally better than the 2nd order upwind scheme which was itself only slightly more accurate than the QUICK scheme. Since the 2nd order upwind scheme had a lower computational cost, and comparable accuracy to the other two, it was the preferred choice. Coupling the pressure and velocity equations improved accuracy and rate of convergence but increased the computational cost; therefore a coupled solver was only used in obtaining an initial solution for the case, with a segregated solver used in the actual computations.

Table 2 Unsteady CFD sensitivity study for a thin flat plate normal to a flow of Re = 5.4×10^4 showing comparisons of various numerical schemes and time step sizes

δt	Advection scheme	Pressure scheme	P-V coupling	Strouhal No	$((C_d)_{CFD} - (C_d)_{expt})/(C_d)_{expt}$
5.0E-03	2nd Order Upwind	Standard	SIMPLE	0.157	35.448%
5.0E-03	1st Order Upwind	Standard	SIMPLE	0.157	15.421%
1.0E-03	1st Order Upwind	Standard	SIMPLE	0.145	15.207%
5.0E-02	1st Order Upwind	Standard	SIMPLE	0.146	13.677%
5.0E-02	1st Order Upwind	Standard	Coupled	0.135	8.981%
5.0E-02	1st Order Upwind	2nd Order	Coupled	0.135	8.981%
5.0E-02	QUICK	2nd Order	Coupled	0.147	15.614%
5.0E-02	2nd Order Upwind	2nd Order	Coupled	0.148	15.087%
5.0E-02	3rd Order MUSCL	2nd Order	Coupled	0.135	14.283%

To improve the accuracy, a time-step 5×10^{-4} seconds was used for the 2D simulations while in the 3D simulations a 5×10^{-3} second time step was sufficient. The SIMPLE and PISO schemes gave similar results and so a SIMPLE algorithm was used.

CFD Simulations were performed considering the flat plate in any of four states;

a) **Static:** With the plate held fixed against translation or rotations
b) **Forced Rotation:** With the plate held fixed along a given axis through its centre and forced to rotate a specified speed about this axis.
c) **Auto-Rotation:** With the plate fixed along a given axis through its centre but free to rotate about this axis under the influence of fluid forces.
d) **Free-Flight:** With the plate free to undergo combined translation and auto-rotation about any axis in a three-dimensional space under the influence of its own weight and the imposed fluid forces.

The computational domain for the static and auto-rotational simulations is described in Fig. 1. The domain consists of a 1 m (L) square plate, 0.0254 m thick with a mass of 3.0 kg, similar to the instrumented plate used in experiments by Martinez-Vazquez, *et al.* (2009b). The plate is positioned so that its centre is 3.5 L from each of the top, bottom and side boundaries. Therefore, the maximum blockage ratio was 8.16% for both the auto-rotational and static simulations. The plate was supported on a horizontal centroidal axis and was held 3.5 L from the inlet boundary and 9 L from the outlet boundary. For the free-flight simulations, a larger domain was used with the plate at a distance of 75 L from outlet boundary in order to allow an adequate flight range.

The plate was held within a rotating spherical inner volume of radius 1.5 L, which was free to rotate about its centre in order to allow for three dimensional changes in plate orientation which are likely to occur during free-flight. In the free-flight simulations, a larger inner spherical region was used with a radius of 2 L.

The surface of this inner region was connected to the surface of the static outer region through a non-conformal grid interface. In FLUENT, this involves first computing an interior layer of faces which is an intersection between the interface faces from the two zones making up the non-conformal interface boundary. Fluxes across the non-conformal interface are then computed using the faces resulting from the intersection of the two interface zones, not from the interface zone faces themselves (Fluent Inc. 2006).

A quasi-steady modelling approach was taken in order to account for the rotating reference frame in the inner region with a moving mesh. This involved solving the absolute velocity formulation of the Navier-Stokes equations for a steadily rotating reference frame over the inner volume. These

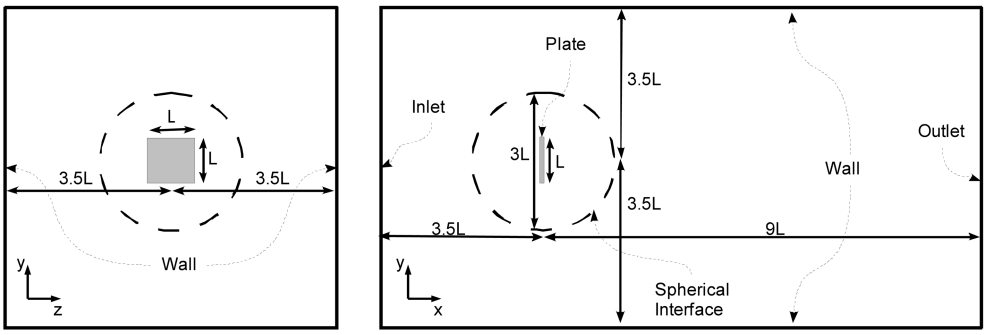

Fig. 1 End and side elevations of domain showing boundaries and dimensions

equations are shown in Eqs. (9), (10) and (11). The linear and rotational velocities of the mesh were computed at the end of each time interval from the RBD model and were assumed to be constant over the subsequent time interval.

$$U_r = U - (\omega \times r) - V_t \tag{9}$$

$$\nabla \cdot U_r = 0 \tag{10}$$

$$\rho \frac{\partial U}{\partial t} + \rho U_r \nabla U + \rho(\omega \times U) = -\nabla P + \nabla \tau \tag{11}$$

where U_r is flow relative velocity vector, U is the flow absolute velocity vector, V_t is the translational velocity vector of the inner mesh region, ω is the rotational velocity vector of the inner mesh region, and r is the position vector from the origin of the rotating reference frame, P is the pressure, and τ is the viscous stress tensor. In the auto-rotational and static simulations, structured hexahedral grids were used for both the inner and outer volumes with approximately 291,000 cells in the domain. In the free flight simulations however the outer region was dynamically meshed using tetrahedral grids at each time step with only the inner region close to the plate meshed as a structured hexahedral grid.

In the static and auto-rotational simulations, the plate, top, bottom and side boundaries were modelled as wall type boundaries with the no-slip condition applied such that the fluid adjacent to the wall boundary moves with the same velocity as the boundary. In the free-flight simulation however, the top, bottom and side boundaries were modelled as free-slip planes to reduce the influence of the boundary on the flow within the domain.

A cubic region around the plate was refined in order to adequately resolve the plate's wall boundary layer as shown in Fig. 2. The first layer of cells close to the plate had a cell spacing of approximately 0.01 m and a mesh grading was applied with a ratio of approximately 1.2 between any two successive cell spacing intervals.

The inlet boundary was modelled as a velocity inlet with flow entering the domain normal to the

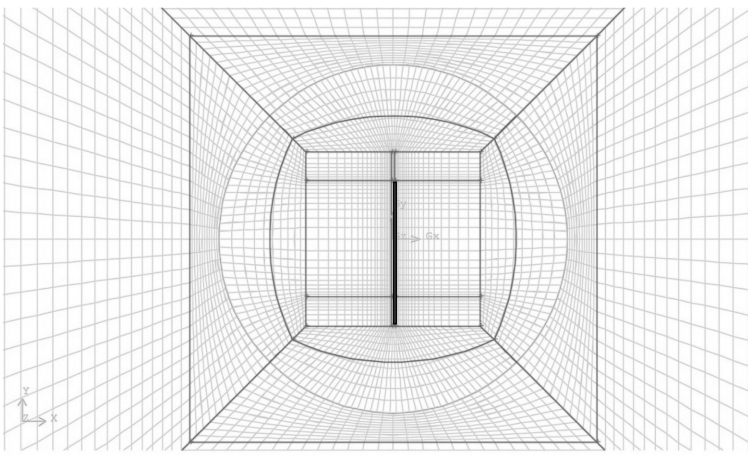

Fig. 2 Section through the 3D mesh showing the meshing of the plate boundary layer and the inner spherical region

inlet face. The inlet velocity was uniform with inlet turbulence described using a turbulence intensity of 1% and length scale of 0.02 m, correspond to typical low turbulence wind tunnel values (ESDU 1970). The outlet was modelled as a pressure outlet, fixed at 0Pa relative pressure with the same turbulence quantities as the inlet. The outlet was positioned sufficiently far from the plate so that no backflow could occur.

Instantaneous aerodynamic forces and moments acting on the plate were computed from the CFD fluid skin friction and pressure acting on the wall boundary representing the plate surface. These forces were decomposed into drag force (x–direction), lift force (y-direction), side force (z-direction) and three component moments about the x, y and z axes through the plate centroid. Additionally, these aerodynamic forces were compared against experimental measurements to help validate the CFD model.

Using the body forces and moments, at each time step a six degree of freedom RBD solver described in section II computes the translation and rotation of the plate. This sequential coupling of CFD and RBD accounts for the FSI of the plate and its influence on plate flight and auto-rotation.

3. RBD modelling

Using the applied body forces and moments, the translation and rotation of the plate was calculated, based on the laws of linear and angular momentum conservation. For a three dimensional rigid body with six degrees of freedom, the momentum conservation equations are represented in Eqs. (12) and (13).

$$m\left(\frac{dv_G}{dt}\right) = F_G \tag{12}$$

$$I_P\frac{d\omega_P}{dt} = M_P - \omega_P \times I_P\omega_P \tag{13}$$

where m is the mass of the plate, v_G is the velocity vector of the plate's centre of mass, F_G is vector of applied forces including gravity forces and CFD simulated aerodynamic forces, ω_P is the plate's angular velocity vector, I_P is the plate's mass moment of inertia tensor, and M_P is the plate's rotational moment vector.

v_G and F_G are expressed in the global inertial coordinate system (shown in Fig. 1) in which Eq. (12) representing conservation of the plate's linear momentum is solved. Eq. (13) which represents angular momentum conservation about the plate's centre of mass is solved in a plate-fitted rotating reference frame in which I_P, ω_P and M_P are expressed. Fig. 3, illustrates the global inertial coordinate system (XYZ) and the rotating plate-fitted coordinate system ($X_pY_pZ_p$) with the Euler angles [ϕ, θ, ψ] defining the orientation of the plate-fitted coordinate system indicated. The torque on the plate computed in the CFD code is expressed in the global inertial coordinate system as M_G and must then be transformed into the plate-fitted reference frame according to Eq. (14) using a *Euler rotation matrix*, R, shown in Eq. (15). To update the rotation matrix, the *Euler angle rates*, [$\dot{\phi}$, $\dot{\theta}$, $\dot{\psi}$], are required and these are obtained from the plate's angular velocity ω_p according to Eq. (16).

$$M_P = RM_G \tag{14}$$

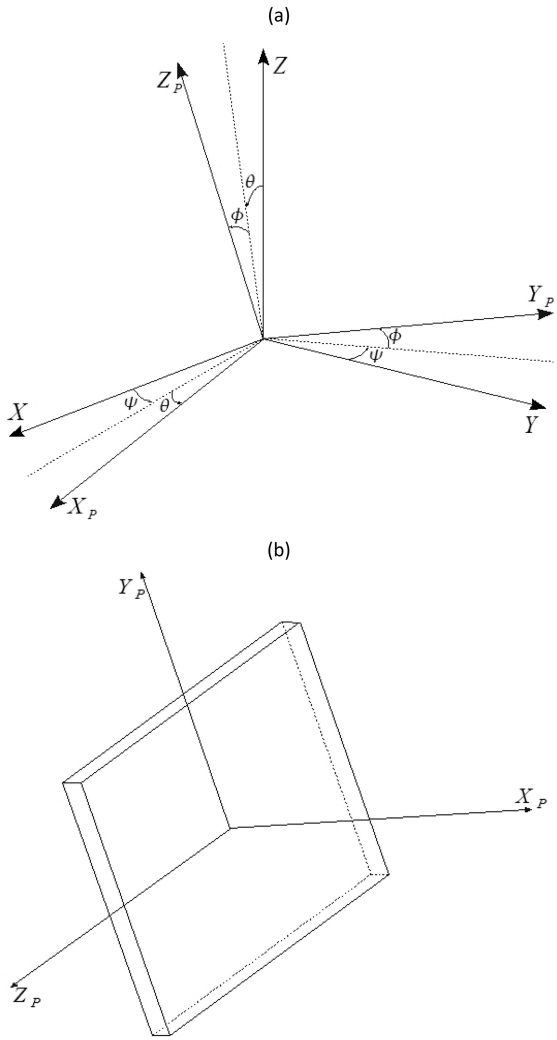

Fig. 3 (a) Illustration of ϕ, θ and ψ the angles defining the orientation of the plate's body-fitted (Xp-Yp-Zp) coordinate system (shown in (b)) with respect to the fixed global (X-Y-Z) coordinate system

$$R = \begin{bmatrix} \cos\theta\cos\psi & \cos\theta\sin\psi & -\sin\theta \\ \sin\phi\sin\theta\cos\psi - \cos\theta\sin\psi & \sin\phi\sin\theta\sin\psi + \cos\phi\cos\psi & \sin\phi\cos\theta \\ \cos\phi\sin\theta\cos\psi + \sin\phi\sin\psi & \cos\phi\sin\theta\sin\psi - \sin\phi\cos\psi & \cos\phi\cos\theta \end{bmatrix} \tag{15}$$

$$\begin{bmatrix} \dot{\phi} \\ \dot{\theta} \\ \dot{\psi} \end{bmatrix} = \begin{bmatrix} 1 & \sin\phi\tan\theta & \cos\phi\tan\theta \\ 0 & \cos\phi & -\sin\phi \\ 0 & \sin\phi\sec\theta & \cos\phi\sec\theta \end{bmatrix} \omega_P \tag{16}$$

With the plate's position and orientation computed, the new instantaneous body forces are then

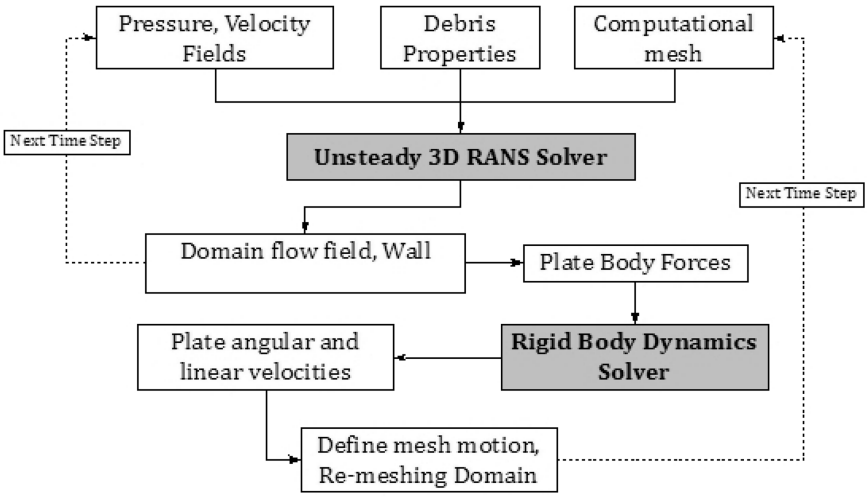

Fig. 4 Sequential coupling of CFD and RBD models to simulate plate auto-rotation and free-flight

computed using the CFD code. Fig. 4 illustrates the sequential coupling of the CFD and RBD codes. The time step was kept small enough to ensure time-step independence of the solution. This sequential coupling of the CFD and RBD codes was found to be computationally efficient and sufficiently accurate for the purposes of this study. The time step size needs to be kept sufficiently small in order to maintain the accuracy of the simulations and the same time step of the order of 5×10^{-3} seconds was used for both the CFD and RBD codes.

4. Static plate simulations

To determine the aerodynamic characteristics of the plate, simulations were performed on a static plate held different angles of attack (pitch) ($0^o - 180^o$) and zero tilt angle (roll and yaw). In this model, the RBD model was not applied. Fig. 5 shows the variation of static force coefficients with angle of attack in a 5 m/s horizontal wind stream.

The CFD static plate simulation results were found to compare well with experimental data from ESDU (1970) for similar plates and Reynolds number range. Drag force is measured as the force in the x-direction while lift force is in the y-direction as defined in Fig. 1. At the stall region, however, the CFD model slightly under-predicts the aerodynamic forces, displaying a less distinct change in force coefficients at the stall angle than in the ESDU (1970) experimental data. Overall however, the body force predictions from the model were found to compare well with experimental results, having a maximum deviation from the experimental values of approximately 10%, which occurs at a 90° angle of attack. This can be attributed to limitations in predicting bluff body flows occurring at this angle of attack using RANS turbulence models.

5. Plate forced rotation simulations

This model has been used to represent the complex FSI phenomena occurring during plate

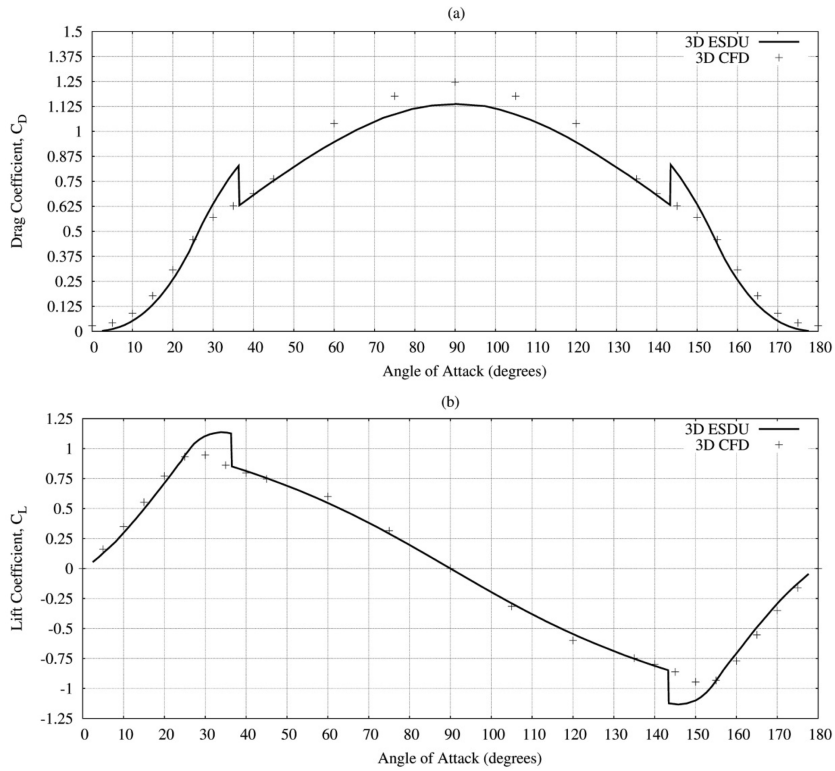

Fig. 5 CFD simulations and experimental data for variation of Drag (a) and Lift (b) coefficients with angle of attack for the plate in a flow of Reynolds Number 3.4×10^5

rotation, and how this affects the plate's force coefficients. Forced rotation simulations were performed with the plate slowly rotated at arbitrarily selected rotational speeds of 5.0, 10.0, 20.0, 40.0 and 80.0 degrees/second about the horizontal axis corresponding to the plate's centre line. This was achieved by rotating the inner spherical meshed volume containing the plate while holding the outer volume fixed. The wall boundary corresponding to the plate surface was rotated along with the inner region. Simulations were performed for several rotational cycles and the results (Fig. 6) were found to be repeatable with no transients.

Fig. 6 shows the instantaneous force coefficients for the rotating plates subjected to forced rotation contrasted against the mean static plate coefficients at similar pitch angles. The horizontal axis contains time normalised using plate rotational speed (in degrees/second) to give the instantaneous angle of attack. An increasingly more pronounced peak in the post stall body forces is observed with increasing plate rotational speed. Compared to the static plate simulations, significantly higher aerodynamic forces are observed with increasing rotational speed. Fig. 7 shows the variation of maximum drag coefficients recorded with rotational speed in a flow of Reynolds number 3.4×10^5. It can be concluded that for the low rotational velocities considered (of the range 0 – 80 degrees/sec), rotational velocity has an effect on the plate body forces that is proportional to the magnitude of the plate's rotational speed. It is also observed that for rotational speeds lower than approximately 0.5 degrees/sec, the maximum drag force is the same as for static plate results. Further investigations are required for rotational speeds up to the plate's stable auto-rotational angular speed, which in

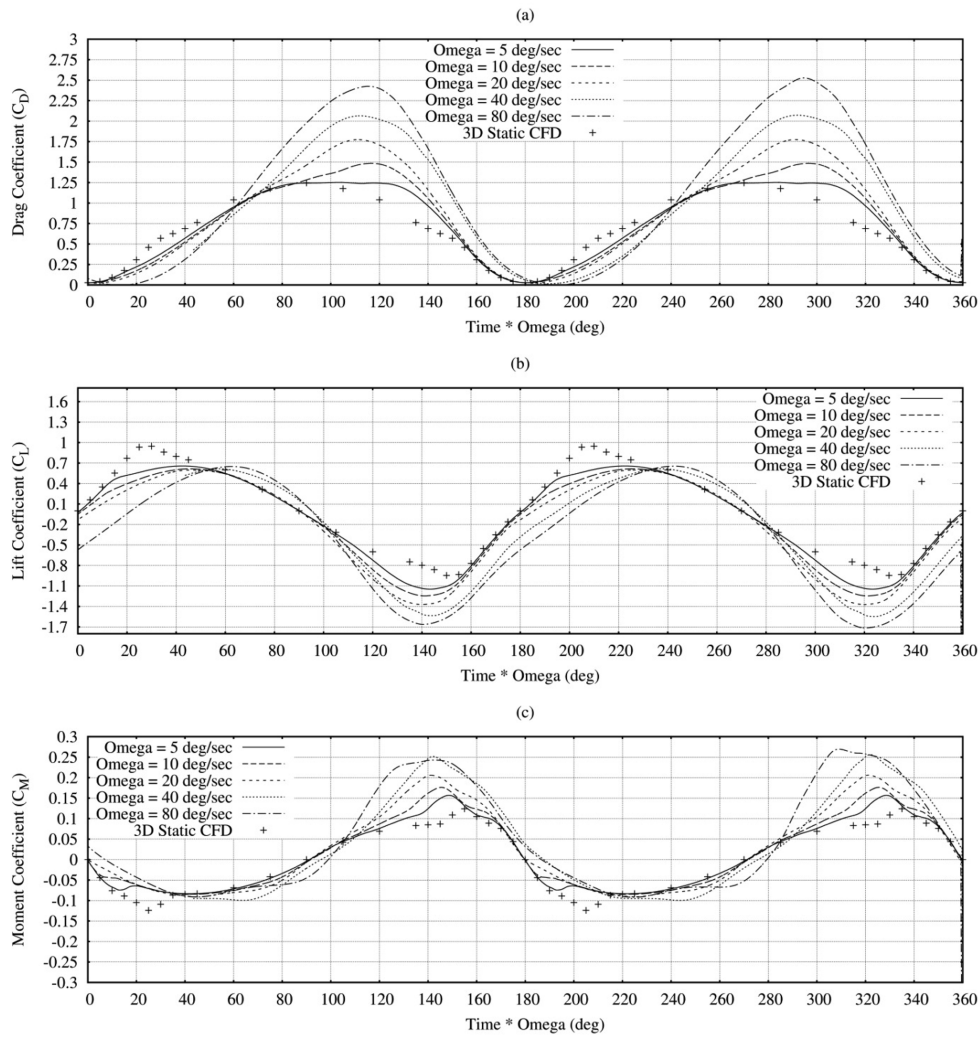

Fig. 6 Plots of drag coefficients (a), lift coefficients (b) and moment coefficients (c) for static and forced rotational simulations performed on a 3D plate at various rotational speeds in a flow of Reynolds Number 3.4×10^5

these flow conditions is approximately 200 degrees/sec (3.5 rad/sec) as shown in Fig. 9(a).

The graph in Fig. 6 also shows that rotating plates exhibit an asymmetry in force coefficients curves about the 90 degree angle of attack position, which is absent in the symmetrical static force curves. For instance, higher drag coefficients are recorded for the same angle of attack when the direction of rotation is causing an increase in angle of attack than when it is causing a decrease in angle of attack. The simulated flow was also noted to reattach at a lower angle of attack when the attack angle is decreasing compared to the angle of attack at which flow separation occurs when the angle of attack is increasing, similar to observations by (Smith 1971). The hysteresis of the force coefficients is a result of the FSI behaviour of rotating plates and has been attributed by Smith (1971) to the delayed reattachment of the separated flow when the angle of attack is decreasing.

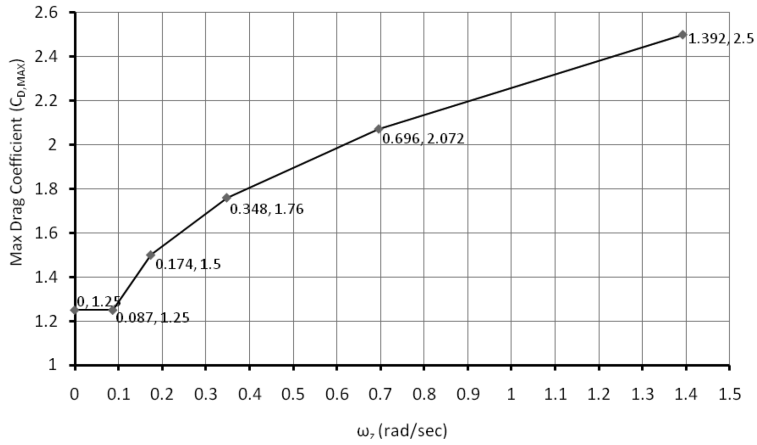

Fig. 7 Variation of maximum drag coefficient ($C_{D,MAX}$) values with rotational speed about the z-axis (ω_z) for low rotational speeds of the range 0 - 0.7 radians/sec (i.e.: 0 - 80.0 degrees/sec)

6. Plate auto-rotational simulations

While the preceding section demonstrates the effects of fixed rotation on the plate's aerodynamic forces, in reality, the plate would not rotate at a fixed speed but would undergo auto-rotation at a rotational speed defined by the problem.

It is therefore of interest to apply the current CFD-RBD model to the simulation of continuous rotation of the plate exposed to an air stream, without external power. This would allow an investigation of the stable auto-rotational behaviour of free-flying plates, how this behaviour is influenced by prevailing wind conditions and its effect on plate body forces.

Simulations were performed on the plate free to rotate about a single fixed horizontal axis through the plate's centroid. These simulations were carried out at wind speeds of 5m/s and 10m/s, which are within the range of wind speeds used from the experimental data used in model validation. Fig. 9 shows the results of these auto-rotational simulations.

Periodic fluctuations in rotational speed are observed, and these are associated with the fluctuation in the moments acting on the plate. This pattern of fluctuating rotational speed continues at a stable frequency corresponding to twice the frequency of plate auto-rotation. Each cycle of rising and falling rotational speed will coincide with a 180 degree half rotation of the plate. The minimum rotational speed is noted to approximately coincide in time with the minimum moment coefficient.

The lift and moment coefficient signals display an asymmetry about their peaks associated with delayed stall and unsteady FSI effects in the plate environment described in previous experimental studies (Smith 1971) and noted in the forced rotation studies in section 5 (Fig. 6) of this paper. Also notable is the simulation of the plate's auto-rotational Magnus lift which results in an elevation of the mean lift force in each rotational cycle to more than zero. Fig. 8 shows contour plots of pressure and velocity magnitude in the plate environments which illustrate the complex interaction between the plate and its wake during auto-rotation.

The prevailing wind speed is also shown to have a strong influence on the intensity of plate rotational speed fluctuations as well as the peak rotational wind speed and the mean speed of stable auto-rotation. Increasing wind speed can be concluded to result in increasing plate auto-rotational speed.

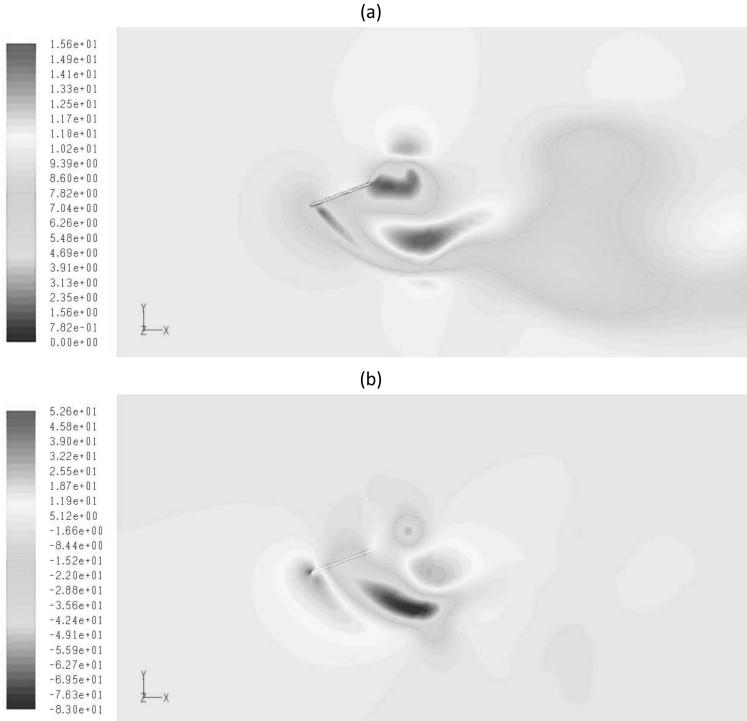

Fig. 8 Contour plots of the simulated flow field around an autorotating flat plate in a 10m/s wind stream showing velocity magnitude (m/s) (a) and pressure (P_a) (b)

Martinez-Vazquez, *et al.* (2009b) have carried out wind tunnel experiments to determine the unsteady pressure field on an auto-rotating plate and the data obtained has been compared against CFD model predictions for model validation purposes. Results are shown in Figs. 8 - 10 and are contrasted against CFD simulations of the current model. Drag coefficients reported by CFD are higher and the peaks appear at pitch angle of 80º and 260º approximately, whilst peak experimental values appear at pitch angles of 90º, 270º. The lift coefficient obtained from the simulation reflects the asymmetries predicted by Tachikawa's (1983) approach, which are however not reflected in the experimental data. With regard to the experimental moment coefficients, these show a more extended region of supporting torque (positive values) which might be explained by bearing friction effects. Moment coefficients reported by CFD simulation resemble those suggested in literature for which a more extended discussion has been provided in Martinez-Vazquez, *et al.* (2009b). The differences showed in Figs. 8 - 10 cannot be fully explained at this point. Whilst the auto-rotational results have certainly been affected in some degree by frictional effects at the bearings, inaccuracies also exist in the CFD-RBD simulation due to numerical errors and limitations in predicting the flow field using RANS turbulence models at moderate and high angles of attack where the plate exhibits stalled and bluff body flows. Fig. 13 shows the experimental lift values compared against CFD lift values with the steady average lift force per cycle deducted to give the $(C_l - \overline{C_l})$ signal. This signal compares better with the experimental data and indicates an over-estimation of the quasi-steady lift force by the CFD simulation.

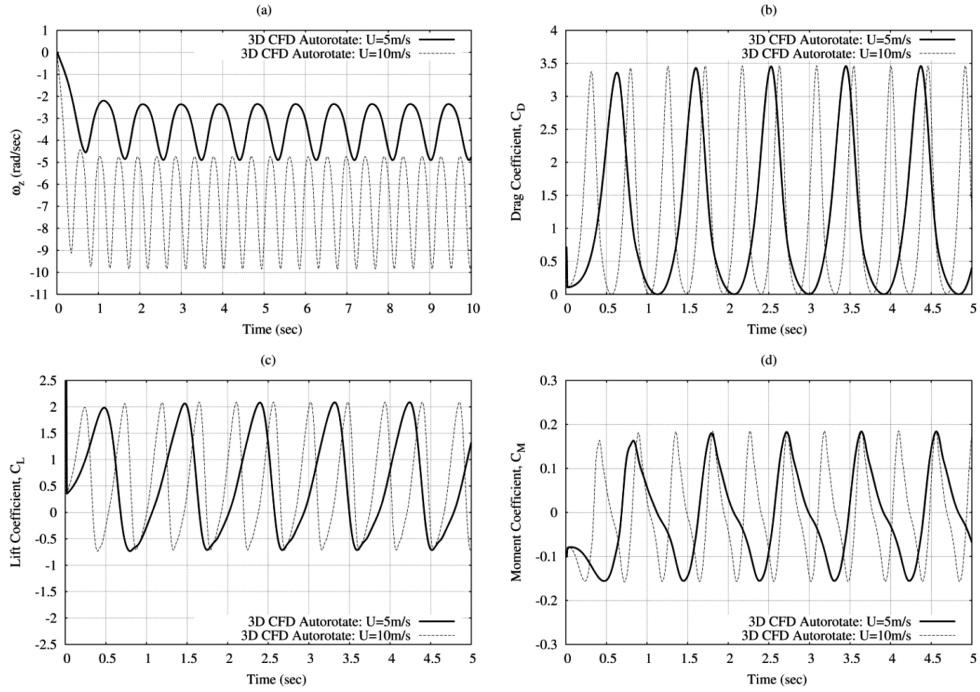

Fig. 9 Time series plots for (a) auto-rotational angular velocity about the z-axis, (b) drag coefficients, (c) lift coefficients, and (d) moment coefficients, on a 3D flat plate in wind streams of 5 m/s and 10 m/s

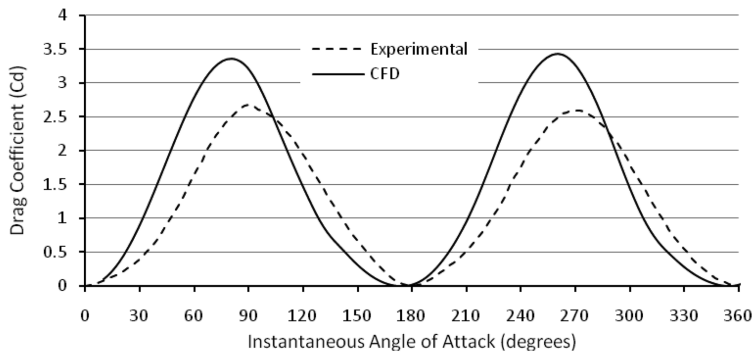

Fig. 10 Experimental and CFD-RBD simulation based drag coefficients for the 3D 1 m square plate of 0.0254 m thickness and 3.0 kg mass, auto-rotating in a 5 m/s wind stream

7. Plate free-flight simulations

Finally the CFD-RBD model was applied to simulating the free-flight of with combined plate translation and auto-rotation under the influence of gravity and aerodynamic forces. A plate free-flight simulation was performed for flight durations of approximately 2.5 seconds and a prevailing wind speed of 20 m/s (in the x-direction). Inlet turbulence intensity and length scale were set to 1% and

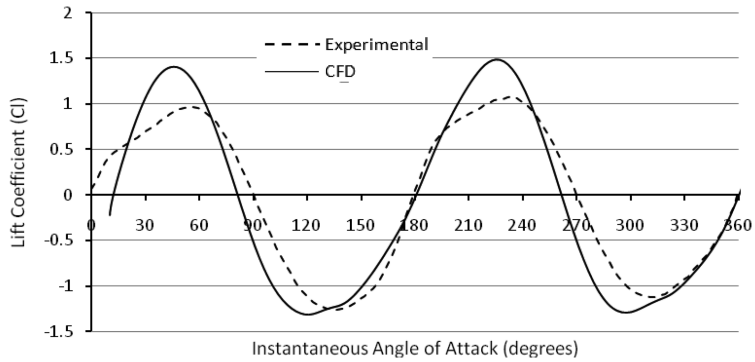

Fig. 11 Experimental and CFD-RBD simulation based lift coefficients for the 3D 1 m square plate of 0.0254 m thickness and 3.0 kg mass, auto-rotating in a 5 m/s wind stream

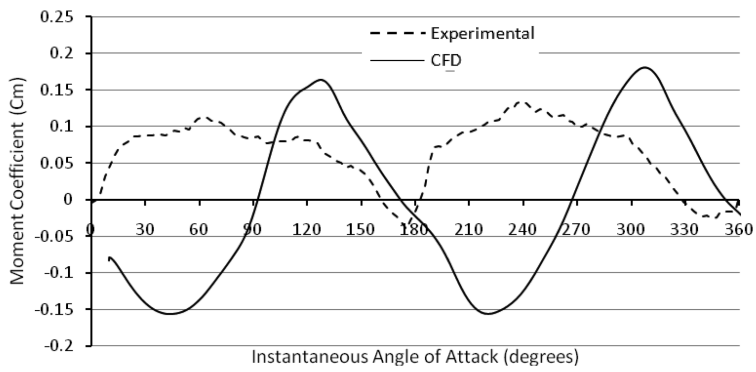

Fig. 12 Experimental and CFD-RBD simulation based moment coefficients for the 3D 1 m square plate of 0.0254 m thickness and 3.0 kg mass, auto-rotating in a 5 m/s wind stream

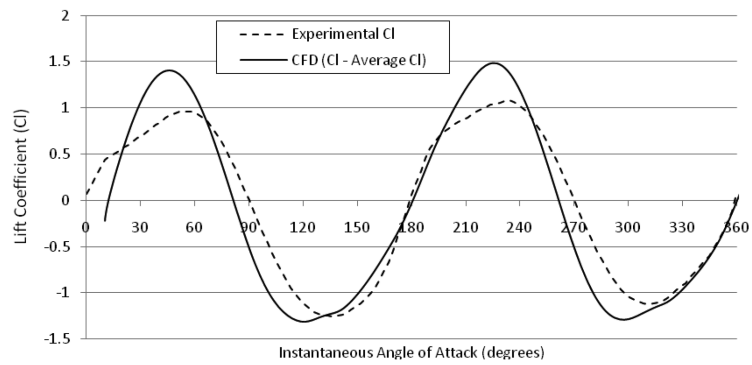

Fig. 13 Experimental and CFD-RBD simulation based lift coefficients for the 3D 1 m square plate of 0.0254 m thickness and 3.0 kg mass, auto-rotating in a 5 m/s wind stream, with the average steady lift deducted from the overall lift measurement to give the $(C_l - \overline{C}_l)$ time series

0.02 m respectively. The RBD code allowed for full six degree of freedom motion of the plate in a three-dimensional space; translation in the x, y and z directions and rotations about each of these axes.

The plate was initially held at a zero tilt (about x-direction) and yaw angles (about z-direction), with a pitch angle of attack (about y-direction) of 30 degrees. As shown in Fig. 14, the resulting plate motion was characterised by significant translations in the vertical (z-direction) and wind direction (x-direction) with relatively negligible motion in the lateral direction normal to the wind (y-direction). Fig. 15 shows the simulated plate position and orientation during free flight for the CFD-RBD model, with significant translations and rotations. A plate trajectory from analytical solutions

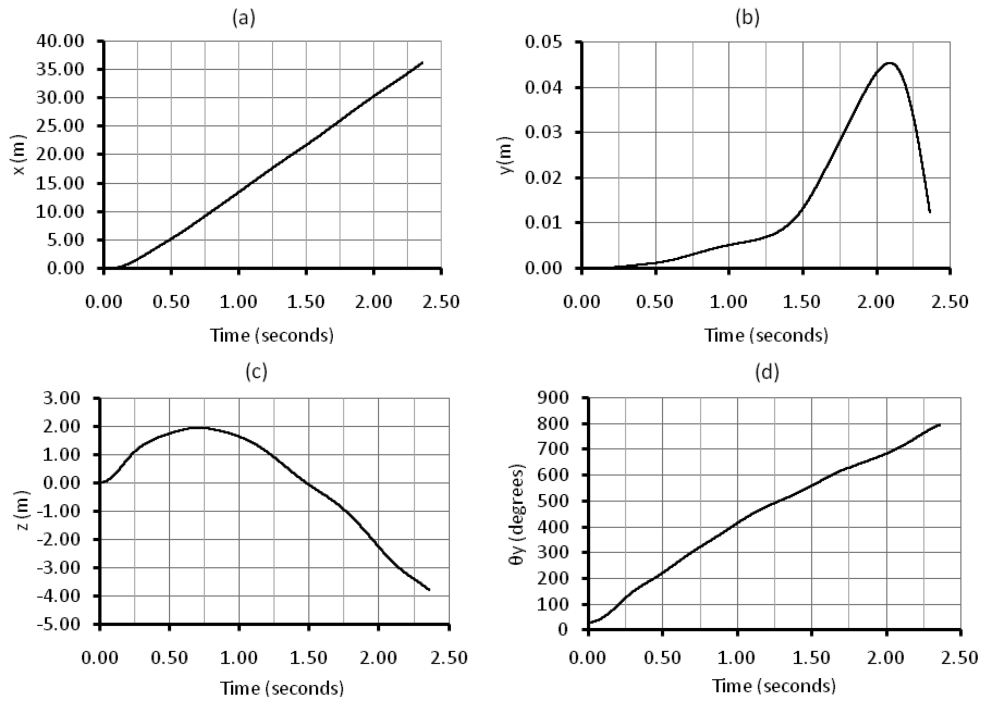

Fig. 14 Time series plots of the x coordinate (a), y coordinate (b) and z coordinate (c) of the plate's centre of gravity, as well as the pitch angle of attack of the plate about the y-axis (d), for CFD-RBD based simulations of plate free-flight

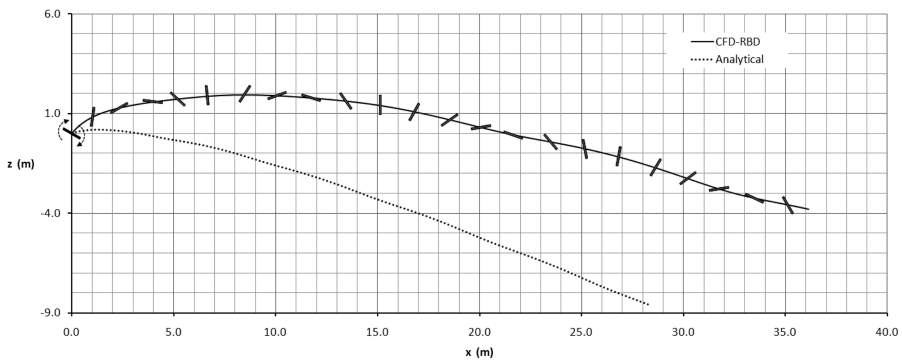

Fig. 15 Simulated CFD-RBD free-flight trajectory compared against trajectory from an analytical solution to the debris flight equations, with illustration of plate orientation and position (taken at 0.1 second time intervals)

to the debris flight equations described in Martinez-Vazquez, *et al.* (2009a) is also shown in Fig. 15 along with the CFD-RBD results. The CFD-RBD simulated direction of rotation is observed to be consistent with experimental observations for free-flying square plates by Tachikawa (1983) shown in Fig. 16.

The CFD-RBD and analytical model trajectories are notably different, and this can be attributed to the treatment of vortex shedding and flow unsteadiness in the plate environment as illustrated in Fig. 18(a). This flow unsteadiness has been found by some studies (Visscher and Kopp 2007) to play a vital role in the initial stages of debris flight by causing strong unsteadiness in the plate's body forces during launch. This unsteady non-uniform nature of the flow is however not captured by existing analytical models of debris flight. The CFD model's more direct treatment of velocity and pressure variations in the flow around the plate and how these affect the plate's motion through non-linear FSI is therefore crucial to the simulation of plate type debris flight.

For the 2.5 second flight time simulated, the plate covered a horizontal range of approximately 36 m (36 L) in the wind direction. The initial launch stage was characterised with the plate being lifted up to approximately 2.0 m (2 L) above its initial position over a range of approximately 9.0 m (9 L), followed by a flight stage. Overall, the 3D CFD-RBD free-flight simulation exhibited behaviour similar to previous 2D CFD-RBD simulations (Fig. 17) such as those described in Kakimpa, *et al.* (2009).

Contour plots of velocity and pressure around the free-flying plate and on its surface were also obtained and illustrate the unsteady flow variations around the plate. Fig. 18(a) clearly shows the simulated velocity magnitude field around the plate at $t = 0.55$ seconds after launch. The lower

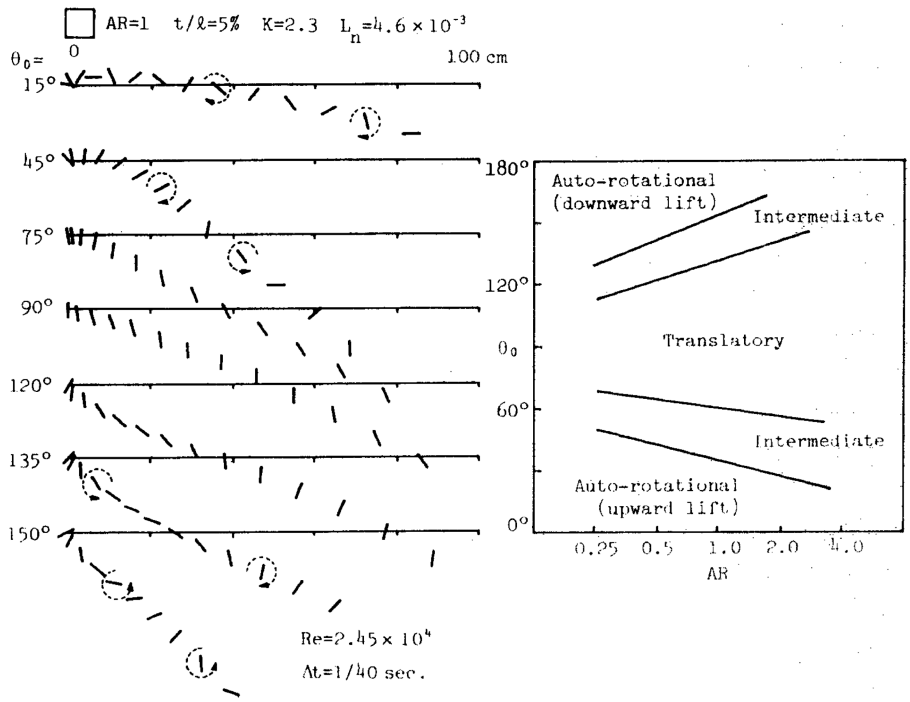

Fig. 16 Experimentally observed changes in a free-flying plate's mode of motion with initial angle of attack (left) and plate aspect ratio (right). Source: Tachikawa (1983)

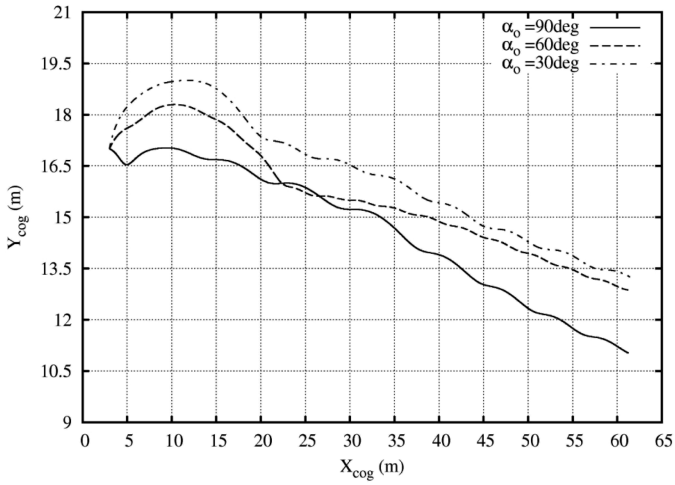

Fig. 17 Simulated 2D CFD-RBD trajectories of a 0.3m square plate of mass 4 kg in a 20 m/s wind stream for 30°, 60° & 90° initial angles of attack (α_o). Y_{cog} is the vertical position of the plate's centre of gravity and X_{cog} is the horizontal position of the plate's centre of gravity

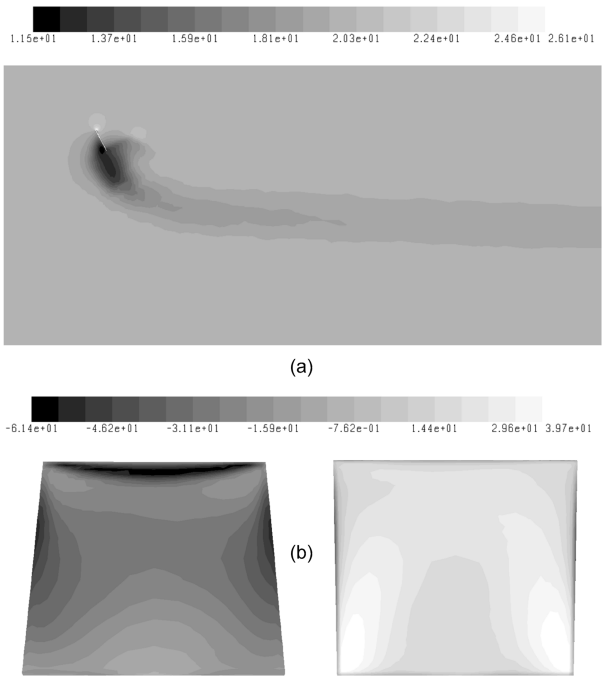

Fig. 18 Contour plots taken at 0.55 seconds after launch showing (a) the velocity magnitude contours on the central plane through the domain, (b) pressure contours on the downstream (left) and upstream (right) faces of the plate viewed normal to the yz plane

velocities observed at the bottom and higher velocities at the top are partly associated with plate blockage effects as well as FSI effects of plate rotation. This field would result in an auto-rotational

lift which would lead to the plate initially rising above its original position and wake as shown in Fig. 18(a). The simulated pressure distribution on the plate, shown in Fig. 18(b), is observed to be fairly symmetrical about the plate's vertical centre line with large positive pressure on the upstream face due to stagnation and negative pressures on the downstream face, especially at the plate edges due to flow separation at these points. This pressure distribution is dependent on the angle of attack and unsteady flow phenomena such as vortex shedding.

8. Conclusions

Coupled CFD and RBD simulations have been demonstrated to hold the potential for economical and efficient investigation of the behaviour of wind borne debris in a variety of debris types and atmospheric conditions. The CFD-RBD framework presented allows for the consideration of unsteady flow effects as well as the temporal and spatial effects of turbulence in the plate environment and how they influence flight behaviour as a result of FSI.

The CFD model has been demonstrated to accurately predict body forces for static flat plates in steady and low turbulence wind stream. Further studies need to be performed on more unsteady and turbulent flow conditions. Rotational speed was shown to have a significant impact on plate body forces that is dependent on the rotational speed. For the CFD turbulence modelling, the 2-equation realisable k-ε turbulence model has been demonstrated to provide adequate performance in streamlined flows at low angles of attack, with less adequate performance at stalling and bluff body flows at moderate and higher angles of attack. Alternative turbulence modelling approaches therefore need to be considered in order to improve the accuracy of the CFD simulations. The simulations presented have considered only low turbulence conditions as well as debris flight in an open domain. Further simulations need to be performed to assess the effects of varied inlet turbulence conditions of environmental scale and effects of plate interaction and behaviour around building wakes and stagnation points.

The CFD-RBD modelling framework has also been demonstrated for simulations of auto-rotational about a single axis. However in reality auto-rotation will not be limited to a single axis but will be three-dimensional in nature therefore the current model needs to be verified for 3D auto-rotational behaviour. The auto-rotational plate body forces obtained for the single axis do show discrepancies with the experimental measurements that need to be further studied.

A plate free-flight simulation test case has also been demonstrated using this model. A further comparison of free flight results with analytical models and free-flight experiments for various initial conditions is recommended to further assess the accuracy of the model for free-flight simulations. This study has also focused on the behaviour of a square flat plate of uniform mass distribution, however the effects of plate shape and mass distribution are vital components of debris flight and need to be assessed through simulations of less idealised debris plates.

References

Baker, C.J. (2007), "The debris flight equations", *J. Wind Eng. Ind. Aerod.*, **95**, 329-353.

Costello, M., Gatto, S. and Sahu, J. (2007), *Using Computational Fluid Dynamics – Rigid Body Dynamic (CFD-RBD) results to generate aerodynamic models for projectile flight simulation*, ARL Paper ARL-TR-4270,

Army Research Laboratory, September 2007.
ESDU (1970), *Fluid Forces and Moments on Flat Plates*, Engineering Science Data Unit – Data Item 70015, London, 1970.
Fluent Inc. (2006), *FLUENT 6.3 Documentation*, 2006.
Holmes, J.D. (2004), "Trajectories of spheres in strong winds with application to wind-borne debris", *J. Wind Eng. Ind. Aerod.*, **92**, 9-22.
Kakimpa, B., Hargreaves, D. and Owen, J.S. (2009), "The flight of wind borne debris: an experimental, analytical, and numerical investigation – part III: CFD simulations", *7th Asia-Pacific Conf. on Wind Engineering*, November 8-12, 2009, Taipei, Taiwan.
Lugt, H.J. (1983), "Autorotation", *Annu. Rev. Fluid Mech.*, **15**, 123-147.
Mann, J., Liu, Y., Kim, Y. and Yue, D.K.P. (2007), "Deterministic and stochastic predictions of motion dynamics of cylindrical mines falling through water", *IEEE J. Oceanic Eng.*, **32**, 21-33.
Martinez-Vazquez, P., Kakimpa, B., Hargreaves, D.M., Baker, C.J., Sterling, M., Quinn, A.D. and Owen, J.S. (2009a), "Predicting the flight of wind borne sheet type debris - an analytical and computational approach", *17th UK Conf. on Computational Mechanics*, 2009, pp. 97-100.
Martinez-Vazquez, P., Baker, C.J., Sterling, M., Quinn, A.D. and Richards, P.J. (2009b), "The Flight of Wind Borne Debris: An Experimental, Analytical, and Numerical Investigation. Part II (Experimental Work)", *7th Asia-Pacific Conf. on Wind Engineering*, November 8-12, 2009, Taipei, Taiwan.
Minor, J.E. (1994), "Windborne debris and the building envelope", *J. Wind Eng. Ind. Aerod.*, **53**, 207-227.
Murman, S.M., Aftosmis, M.J. and Rogers, S.E. (2005), "Characterization of space shuttle ascent debris aerodynamics using CFD methods", *43rd AIAA Aerospace Sciences Meeting*, 2005.
Richards, J.P., Williams, N., Laing, B., McCarty, M. and Pond, M. (2008), "Numerical calculation of the three-dimensional motion of wind-borne debris", *J. Wind Eng. Ind. Aerod.*, **96**, 2188-2202.
Shih, T.H., Zhu, J. and Lumley, J.L. (1995), "A new Reynolds stress algebraic equation model", *Comput. Method Appl. M.*, **125**, 287-302.
Skews, B.W. (1990), "Autorotation of rectangular plates", *J. Fluid Mech.*, **217**, 33-40.
Smith, E.H. (1971), "Autorotating wings: an experimental investigation", *J. Fluid Mech.*, **50**, 513-534.
Tachikawa, M. (1983), "Trajectories of flat plates in uniform flow with application to wind-generated missiles", *J. Wind Eng. Ind. Aerod.*, **14**, 443-453.
Visscher, B.T. and Kopp, G.A. (2007), "Trajectories of roof sheathing panels under high winds", *J. Wind Eng. Ind. Aerod.*, **95,** 697-713.